ACS APPLIED MATERIALS & INTERFACES

Research Article

Cite This: ACS Appl. Mater. Interfaces 2019, 11, 41717−41725

www.acsami.org

High-Speed Photothermal Patterning of Doped Polymer Films

Zhengliang Su,[†] Zaira I. Bedolla-Valdez,[‡] Letian Wang,[†] Yoonsoo Rho,[†] Sunny Chen,[†] Goktug Gonel,[‡] Eric N. Taurone,[‡] Adam J. Moulé,[*,‡] and Costas P. Grigoropoulos[*,†]

[†]Department of Mechanical Engineering, University of California, Berkeley, 94720 California, United States

[‡]Department of Chemical Engineering, University of California, Davis, 95616 California, United States

Supporting Information

ABSTRACT: Organic semiconductors (OSCs) offer a new avenue to the next-generation electronics, but the lack of a scalable and inexpensive nanoscale patterning/deposition technique still limits their use in electronic applications. Recently, a new lithographic etching technique has been introduced that uses molecular dopants to reduce semiconducting polymer solubility in solvents and a direct-write laser to remove dopants locally, enabling rapid OSC etching with diffraction limited resolution. Previous publications postulated that the reaction that enables patterning is a photochemical reaction between photoexcited dopants with neutral solvent molecules. In this work, we analyze the photoinduced dissolution kinetics of F4TCNQ doped P3HT films using time-resolved in situ optical probing. We find two competing mechanisms that control de-doping and dissolution: the first is the photochemical reaction posited in the literature, and the second involves direct heating of the polymer by the laser, inducing increased solubility for both the polymer and dopant. We show that the wavelength-specific photochemical effect is dominant in low photon doses while the photothermal effect is dominant with high excitation rates regardless of laser wavelength. With sufficiently high optical intensity input, the photothermal mechanism can in principle achieve a high writing speed up to 1 m/s. Our findings bring new insights into the mechanisms behind laser direct writing of OSCs based on dopant induced solubility control and enable ultraprecise fabrications of various device configurations in large-scale manufacturing.

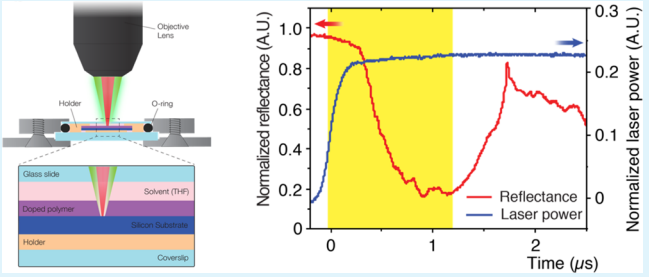

KEYWORDS: *organic semiconducting materials, photothermal effect, laser direct writing, in situ optical probing, scalable manufacturing*

INTRODUCTION

The last two decades have witnessed the burgeoning development in organic electronics. Compared to the state of the art complementary metal oxide silicon (CMOS) technology, the most overwhelming advantages offered by organic semiconductors (OSCs) include easy access to chemical tuning of material properties, better compatibility to large-area biointegrated flexible electronics, and high potential toward scalable and inexpensive manufacturing.[1−11] Among all the proposed material candidates for OSCs, polymeric semiconducting materials have received much higher attention due to their unparalleled diversity and extraordinarily wide tuning range of physical and chemical properties. For example, semiconducting polymers are lightweight and mechanically flexible, coat well over large areas, and can be chemically tuned for specific applications such as light emission, charge separation, high mobility, and biocompatibility.[12−17]

Although much progress in polymeric electronics has been achieved, finding a practical and reliable nanomanufacturing process with high throughput and low cost still remains a challenge. Organic materials, particularly polymers, are in general incompatible with the CMOS fabrication platform. For example, many polymers may mix with the photoresists or dissolve into the strip solutions.[1] Current available fabrication techniques for patterning organic semiconducting materials include vacuum deposition, ink-jet printing, imprinting and stamping, and photolithography. However, these techniques are all subject to severe limitations. Vacuum deposition is only feasible for small molecule materials and hence cannot be applied to the large family of polymer materials.[2] Ink-jet printing is constrained by limited resolution, mainly determined by the rheological characteristics of the material ink and the needle size.[18−20] Imprinting and stamping suffer from the instability and deformation of materials; thus, their reliability and efficiency are always costly to address.[21−25] Photolithography requires prolonged processing steps, some of which may compromise the chemical and physical properties of the organic materials.[30] Therefore, an inexpensive, convenient, scalable nanopatterning technique for OSCs is critically needed to enable further development of organic electronic device applications.

Received: September 3, 2019
Accepted: October 17, 2019
Published: October 17, 2019

DOI: 10.1021/acsami.9b15860
ACS Appl. Mater. Interfaces 2019, 11, 41717−41725

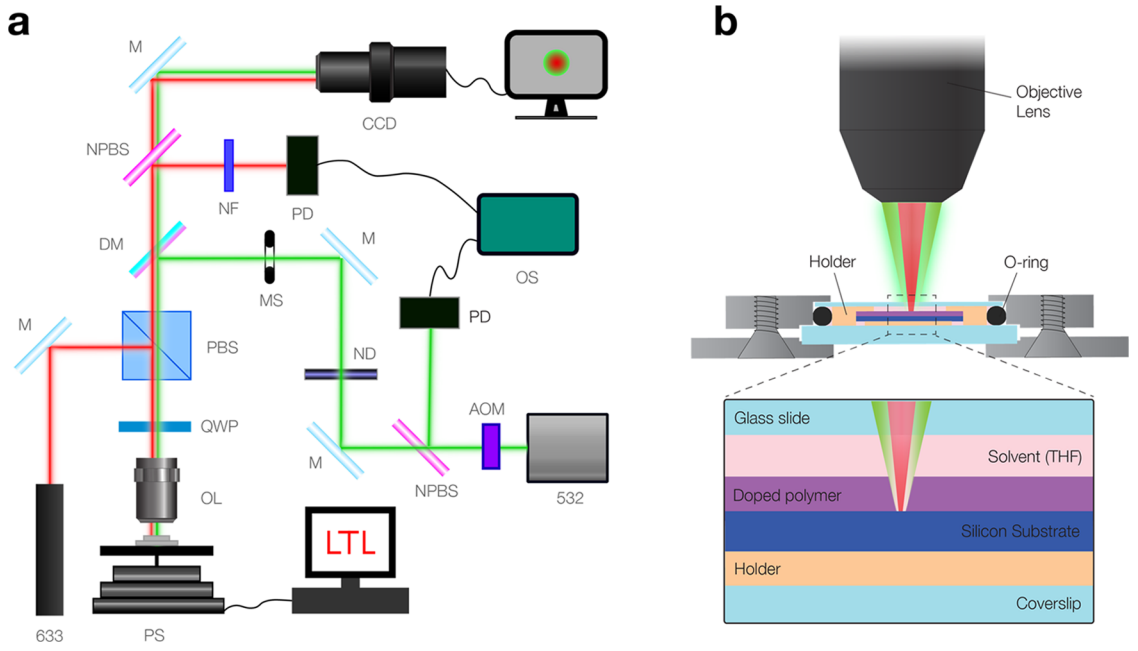

Figure 1. Time-resolved in situ optical probing setup. (a) 532 nm processing laser (532) passes through an acousto-optic modulator (AOM) and is split by a nonpolarized beam splitter (NPBS). The minor branch is collected by a photodetector (PD), and the major is delivered through a neutral density filter (ND) and a mechanical shutter (MS), reflected off a dichroic mirror (DM), and then focused by a 10× objective lens (OL) onto the sample (SM). The s-polarized 633 nm probing laser (633) is reflected off a polarized beam splitter (PBS), through a quarter wave plate (QWP), focused through the OL onto the sample. The reflected light from the sample is collected by the OL, passing the QWP again, becomes p-polarized, and is transmitted through the PBS; the signal passes a 532 nm notch filter (NF) and is collected by another PD. The signals from the two PDs are sent to and synchronized by an oscilloscope (OS). The sample is mounted on a nanopositioning piezo stage (PS). A charge-coupled device (CCD) camera system is coupled with the transmitted light through the DM and NPBS. (b) Enlargement of the solvent cell showing the sample details.

Alternatively, laser-assisted material processing is a versatile and noncontact patterning tool for many inorganic materials and is ideal for scalable and inexpensive manufacturing. However, traditional laser etching is caused by large thermal changes, such as ablation, melting, and vaporization, and for organic materials, this could lead to severe degradation of properties, such as carbonization, oxidization, and deformation. Petsch et al. used pulsed laser patterning to make organic photovoltaic devices. With traditional laser etching, the smallest negative features that could be achieved were ∼20 μm, with another 2−3 μm of the polymer showing clear signs of degradation, dewetting, melting, and removal.[35]

Recently, Moulé et al. have developed a novel patterning technique, called dopant-induced solubility control (DISC), based on the observation that the solubilities of some semiconducting polymers, for example, the prototypical semiconducting polymer regioregular poly(3-hexylthiophene) (P3HT), can be reversibly controlled by doping with high electron affinity molecules (such as the molecular dopant 2,3,5,6-tetrafluoro-7,7,8,8-tetracyanoquinodimethane (F4TCNQ)).[1−3] The solubility reduction of the semiconducting polymer upon doping is believed to result from the formation of the ionic salt complex, [polymer$^+$]:[dopant$^-$], which is not soluble in nonpolar solvents.[2] The salt complex formation can be reversed upon exposure to photons with certain energy in a bath of good solvent for the polymer.[3] Therefore, in the presence of a good solvent for both neutral polymer and dopants, such as tetrahydrofuran (THF) for P3HT and F4TCNQ, a laser of specific wavelength (405 nm for P3HT:F4TCNQ) can be utilized to dissolve the doped polymer locally, resulting in the patterning capability with beyond-diffraction-limited resolution.[1−3] This irreversible process is attributed to the photon-induced transition from the [polymer$^+$]:[dopant$^-$] complex to neutral polymer and dopants.[3] Thus, using a combination of DISC and laser excitation for etching reduces the laser power needed to etch by several orders of magnitude while increasing the pattern resolution from >20 μm to <400 nm. This technique has most of the useful features of photolithography, whereas here, the polymer essentially acts as its own photoresist. Thus, the proposed protocol is compatible with current photolithography techniques but requires fewer steps and no corrosive chemicals.[26−32] This method can be easily applied for a variety of polymeric materials (relevant work will be published soon) and therefore has high potential to be widely used and to give an impact to the organic electronics industry. The ability to directly control both film morphology and doping level with diffraction-limited resolution will make DISC, combined with low-power laser etching, a strong method in the fabrication of integrated organic electronic devices. Despite the promising preliminary studies about DISC patterning, the proposed etching mechanism is incomplete; the role of the photon-induced de-doping process has not been quantified, and temperature changes while etching have not even been considered. In short, a very promising patterning technique has been proposed, but the thermodynamics and kinetics of the process have not been reported or quantified to allow general use of laser-assisted DISC patterning.

In this work, we study the etching mechanisms by examining the purely photothermal effect on the dissolution of the P3HT:F4TCNQ thin film immersed in a good solvent (THF), by means of a time-resolved in situ optical probing technique. Note that the photochemical de-doping effect in P3HT-F4TCNQ films occurs exclusively upon irradiation with near

DOI: 10.1021/acsami.9b15860
ACS Appl. Mater. Interfaces 2019, 11, 41717−41725

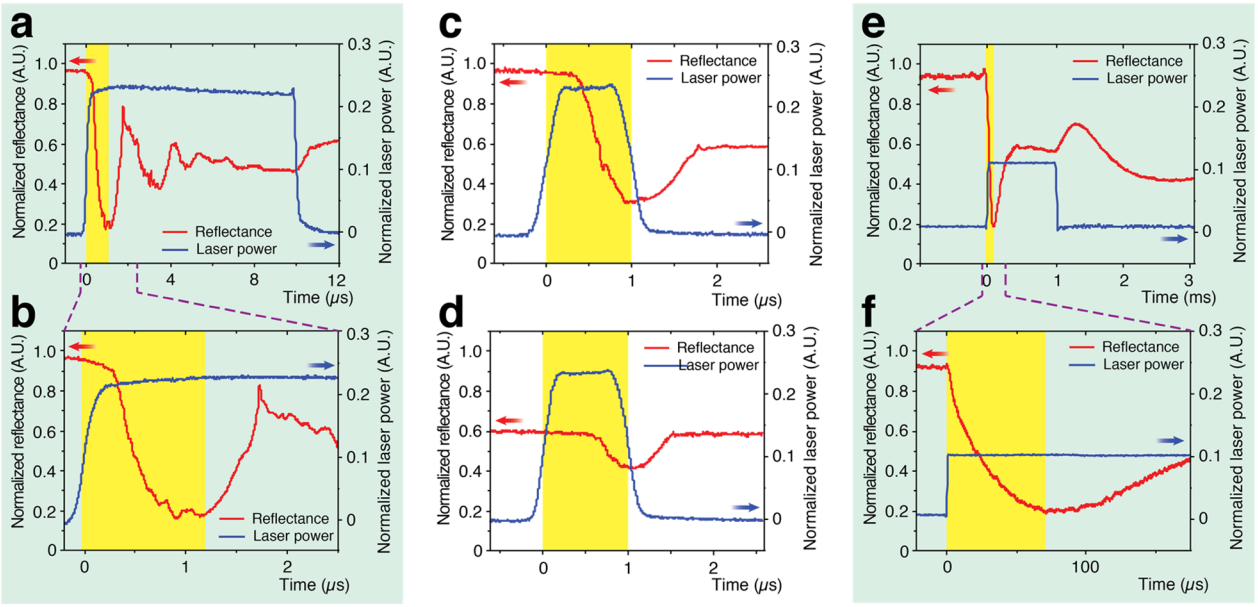

Figure 2. Results of time-resolved in situ optical probing. The dynamic response of the system upon exposure to 532 nm laser irradiation is characterized by the reflectance of the 633 nm laser signal (red traces), of which the initial drops (indicated by the yellow shadows) represent the dissolution process of the P3HT:F4TCNQ thin film within the probed region. Blue traces indicate the signal from the photodetector that collects the minor branch of the 532 nm processing laser, as a time reference. (a) Typical reflectance response of the system under high laser power (40 mW, 10 μs) with the enlargement (b) of the reflectance response, showing that the temperature-induced dissolution process takes 1.2 μs. (c,d) Reflectance response of the system to 532 nm laser pulses with a power of 40 mW and duration of 1 μs, verifying that the time needed for full dissolution is more than 1 μs. The first 1 μs pulse (c) induces a similar response, and the initial drop magnitude is close to but smaller than that of the 10 μs pulse case (87%). The second 1 μs pulse (d) also induces an observable drop, indicating that the first 1 μs pulse does not support the full dissolution of the probed region. (e) Typical reflectance response of the system upon exposure to low-intensity laser irradiation. The processing laser used is 15 mW, and the pulse duration is 1 ms. (f) The enlargement of the reflectance response in panel (e), showing that it takes around 70 μs for the dissolution process to finish.

405 nm light.[2,3] Therefore, interpretation of etch rate data is difficult because 405 nm laser irradiation causes both photochemical removal of F4TCNQ and temperature increases in both polymer and dopant dissolution ($\Delta G_{mix} \approx -T\Delta S$). In contrast to previous studies that all used a 405 nm laser for patterning, we use 532 nm laser irradiation so that we can isolate the photothermal effect only and thus determine how laser power affects the dissolution rate for both mechanisms with a heat transfer model. Our work shows that the wavelength-specific photochemical effect (photon-induced de-doping) is dominant for low laser intensities, while for high laser excitation rates the photothermal effect dominates the etch rate independent of wavelength. With relatively high laser fluences, the photothermal mechanism is able to realize a high writing speed up to 1 m/s in principle.

Our work not only brings new fundamental understanding in light−material interactions that play important roles in advanced laser processing but also gives valuable directions for large-scale and inexpensive manufacturing of organic electronics based on the DISC laser direct writing technique. Besides, the scientific methodology utilized here, in situ optical probing, provides high temporal (~1 ns) and spatial (~1 μm) resolution for characterizing dynamic processes in laser manufacturing and processing (laser-induced crystallization/solidification, laser thinning, laser annealing) and can be easily extended to other applications, such as imaging elastic wave propagation in solids, measuring photon-initiated chemical reaction rates, and decoupling thermal effects in multi-physics phenomena.[33]

RESULTS AND DISCUSSION

The time-resolved in situ optical probing is performed to investigate the dynamics of the dissolution process of the P3HT:F4CTNQ thin film immersed in THF upon the 532 nm laser irradiation; hence, only dissolution induced by the photothermal effect is measured. As shown in Figure 1, a dual-beam strategy is utilized for simultaneous processing and probing. A laser pulse with duration from 100 ns to 1 ms of a 532 nm continuous-wave (CW) laser generated by an acousto-optic modulator (AOM) is focused onto the P3HT:F4TCNQ thin film, initiating the photothermal dissolution, and a 633 nm CW laser is used as the simultaneous probing, of which the reflectance as a function of time is recorded to characterize the dynamics of the dissolution (see the Experimental Section). The processing laser power used in this study varies from 1 to 50 mW (measured after the objective lens), and the probing laser power is kept at 0.1 mW. The heating effect from the probing laser light at such a power level is negligible since the maximum local temperature increase of the sample is well below 1 K from the simulation, and there is no observable change of the film upon exposure to the probing laser at the timescale of minutes, while the measurement timescale of all the experiments is within 1 ms. Both of the two laser beams show a good Gaussian profile in the cross section; the knife edge measurement shows that the beam waists are 12 and 10 μm in diameter for the processing laser and the probing laser, respectively (Figure S1). During the experiments, the two laser beams are aligned so that the spot of the 633 nm probing laser is fully enclosed by that of the 532 nm processing laser; thus,

DOI: 10.1021/acsami.9b15860
ACS Appl. Mater. Interfaces 2019, 11, 41717−41725

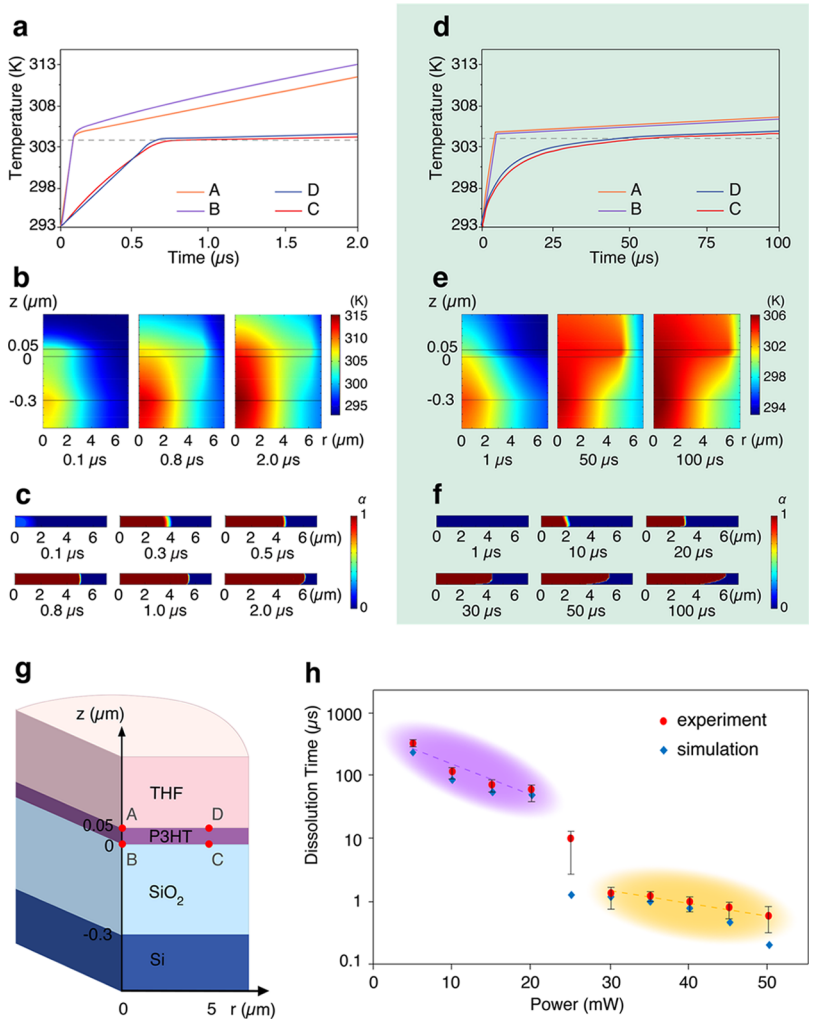

Figure 3. Simulation results of the pure thermal effect. (a–c) Results of the fast dissolution with high processing laser power (40 mW). (a) Temperature history at specified locations in the P3HT:F4TCNQ film: (r, z) = (0, 0.05) μm (orange line), (0, 0) μm (purple line), (5, 0) μm (red line), and (5, 0.05) μm (blue line), corresponding to points A, B, C, and D illustrated in panel (g), respectively. (b) Temperature field profiles at specified times, from left to right: 0.1, 0.8, and 2.0 μs. (c) Phase distribution profiles at specified time, showing the phase transition evolution, from left to right: (top line) 0.1, 0.3, and 0.5 μs; (bottom line) 0.8, 1.0, and 2.0 μs. (d–f) Results of the slow dissolution with low processing laser power (15 mW). (g) Schematics of the solvent/P3HT/SiO_2/Si multilayer model system in a cylindrical coordinate. (h) Experimental and simulation results for the whole range of laser powers used in our experiment, both showing two distinct scales of dissolution time (indicated by the shadowed regions) corresponding to high and low laser powers; the experimental data is the average of 10 repeated experiments for each power, and the error bars denote the standard deviations; the dashed lines serve as guides for the eye.

the signal from the reflected 633 nm light fully indicates the dynamic change within the processed region.

Figure 2 shows the experimental results of the time-resolved in situ optical probing of the photothermal dissolution of P3HT:F4TCNQ thin films immersed in THF. The blue traces illustrate the signal from the photodetector that collects the minor branch of the 532 nm processing laser, as a time reference for the initiation of the dissolution. The reflectance signal of 633 nm light (red traces) characterizes the dynamic response of the substrate-polymer-dopant-solvent system upon exposure to 532 nm laser irradiation. The initial drops in reflectance (indicated by the yellow shadows) represent the photothermal dissolution process of the P3HT:F4TCNQ thin film, from which the dissolution rate can be calculated. One of the typical system response profiles is illustrated in Figure 2a: the onset of the 532 nm CW laser, indicated by the instantaneous increase of the blue trace at time 0, triggers the system response, initiating a sharp drop of the reflectance signal lasting from 0 to 1.2 μs (see the enlargement in Figure 2b) followed by a quasi-sinusoidal fluctuation with an exponentially decaying amplitude. Such fluctuation may result from the local hydrodynamic instability of the solvent near the dissolved region due to the instantaneous thermodynamic change upon the processing laser irradiation (sharp temperature and pressure rise) and/or the dissolution of the material into solvent. The localized motion of the solvent deflects the reflected 633 nm laser beam and alters the amount of the 633 nm light collected by the objective lens. It takes 5–10 μs before this fluctuation fades away, and the signal reaches a plateau. When the irradiation of the 532 nm laser is turned off, the reflectance signal experiences some fluctuation again due to an instantaneous thermodynamic change and then returns to the final plateau. Analysis of the reflection signal after complete dissolution is beyond the scope of this paper.

The thermal dissolution process can happen on two distinct timescales, corresponding to two thermal dissolution rates.

DOI: 10.1021/acsami.9b15860
ACS Appl. Mater. Interfaces 2019, 11, 41717–41725

When the etching laser power is high, typically larger than 30 mW in our experiment (corresponding to an average intensity of 27 kW/cm^2), the thermal dissolution process occurs within ~1 μs, corresponding to a thermal dissolution rate on the order of 10 μm^3/μs or higher. As shown in Figure 2b, where the processing laser power is 40 mW and the exposure duration is 10 μs (FWHM), the full dissolution of the probed region (within the 10 μm in diameter spot of the 633 nm laser) takes 1.2 μs, corresponding to a thermal dissolution rate of 16 μm^3/μs. To verify that the time needed for full dissolution of the probed region is more than 1 μs, a shorter duration (1 μs) of laser with the same power (40 mW) is used to heat the sample twice sequentially at the same location. The first 1 μs pulse (Figure 2c) induces a response similar to that of the 10 μs pulse case (Figure 2a), but the initial drop magnitude is smaller (87%). The second 1 μs pulse (Figure 2d) also induces an observable reflectance response, indicating that the first 1 μs pulse did not fully dissolve the probed region. During the second 1 μs pulse, there is a longer delay between the onset of irradiation and the onset of dissolution (~0.6 μs) than for the first pulse (~0.3 μs). The slower response for the second pulse could be attributed to the extra binding force between the polymer and substrate or to the reduced absorbance in a thinner layer. The slower dissolution of the P3HT near the substrate was also noted in a previous publication.[2]

On the other hand, when the etching laser power is low, smaller than 20 mW (corresponding to an average intensity of 17.6 kW/cm^2), thermal dissolution requires tens of μs or longer, corresponding to a thermal dissolution rate on the order of 1 μm^3/μs or lower. As shown in Figure 2e,f, when 15 mW laser power is used, the full dissolution of the P3HT:F4TCNQ thin film within the probed region takes around 70 μs and the corresponding thermal dissolution rate is 0.28 μm^3/μs. Such a large difference in the thermal dissolution timescale is due to the fact that the temperature time course has two distinct stages. The first period is a fast increase, of which the rate of change is correlated to the heating power, and the second is a much more gradual rise due to the quasi-balance between the heat generation and the heat diffusion to the adjacent media. Such a temperature time course profile is typical in laser processing and in many other physical processes controlled by heat transfer.[28,29] When the laser power is high, the full dissolution finishes during the fast response stage, resulting in a fast dissolution within ~1 μs. Meanwhile, in the case of low laser power, the initial fast response cannot efficiently remove the material from the probed region and the full dissolution can only finish at the second stage, thus leading to a much larger timescale (>50 μs).

To better understand the thermal mechanism, we performed steady heating experiments showing that the phase change involved in the thermal dissolution of the P3HT:F4TCNQ thin film into THF takes place at a temperature of ~304 K (Figure S4). To verify that the temperature rise is also the major driving force for dissolution during the nonequilibrium transient laser heating experiment above, we utilized a commercial finite-element-analysis package (Comsol Multiphysics, 5.3a) to simulate the laser-induced thermal effect involved in the dissolution. The thermal modeling is based on a temperature-threshold irreversible phase transition method; namely, once the temperature of any local finite element of the P3HT:F4TCNQ film reaches the temperature threshold, 304 K, it undergoes an instantaneous irreversible transition to a state with the same material parameters as the solvent, corresponding to the irreversible dissolution process. There are two separate heat sources: one is the absorbance in the P3HT:F4TCNQ thin film itself, and the other comes from the absorbance in the silicon substrate. The latter is simplified by a surface heat flux on the interface between the silicon dioxide layer and the silicon substrate, since the surface heat flux has little contribution to the film dissolution process (Figure S5), and the effect will be even less if the heat source is distributed in the finite volume defined by the skin depth of silicon. Note that both heating sources have a Gaussian distribution on the cross section; the 99% intensity half-width is 6 μm, corresponding to the laser focus waist of 12 μm in diameter. As the simulation proceeds, once a local polymer element transforms, this element does not generate heating power anymore (corresponding to the fact that the absorbance of the dissolved materials is adequately negligible). The heating powers of the two heat sources are calculated from an optical transfer matrix method,[36] based on the refractive indices and extinction coefficients of the materials measured by ellipsometry (Figures S2 and S3). In the simulation, the fluid motion of the solvent is neglected due to the extremely small Rayleigh number (~10^{-7}), which justifies that the heat transfer in the solvent is mainly in the form of conduction, rather than convection (Table S2). The time interval used in the simulation is one-thousandth of the total simulated time range.

Figure 3 shows the simulation results comparing the temperature and phase transition evolution between fast (a–c) and slow (d–f) dissolution processes. Figure 3a,d shows the temperature time courses probed at specified locations (A–D) in the solvent/P3HT/SiO_2/Si multilayer model system (Figure 3g). Positions A, B, C, and D correspond to position notations (r, z) = (0, 0.05), (0, 0), (5, 0), and (5, 0.05) in the unit of μm in a cylindrical coordinate system, which confine the region of interest corresponding to the probed region in experiments. Due to the cross-sectional Gaussian distribution of the heating powers, points on the probe boundary at r = 5 μm have the slowest responses among all the elements within the probed region. Therefore, the correspondence to the experimental results is straightforward: the time that it takes for the temperature of the boundary points to reach the threshold, 304 K, denoted by the gray dashed line, is equivalent to the time of the initial drop of the reflectance in experiments since all the material within the probed region is dissolved. The simulation shows that the full thermal dissolution of the probed region takes around 0.8 μs for a 40 mW laser, while it takes around 55 μs for a 15 mW laser. The results agree reasonably well with the experimental values, 1.2 and 70 μs, respectively. These simulation results support the above heat transfer reasoning: the temperature evolution induced by a constant heat source usually shows a fast and instantaneous increase and a following slow and steady rise. The fast increase is due to the nonequilibrium between the abrupt release of thermal energy and the sluggish heat diffusion in the form of conduction. The photon energy thermalization to the thermal energy carriers (electrons and phonons) in solids occurs within a few picoseconds (10^{-12} s), but the collective transport of excited thermal energy carriers, which is the microscopic mechanism of heat conduction, needs much longer time. That is, the thermal energy is not efficiently transported from the irradiated region to its surroundings (including the nonirradiated P3HT region and the media, THF and SiO_2) in the beginning, which accounts for the initial fast increase. The timescale for efficient heat diffusion to balance the energy release can be estimated

DOI: 10.1021/acsami.9b15860
ACS Appl. Mater. Interfaces 2019, 11, 41717–41725

by the characteristic heat diffusion time $\tau \sim \frac{l^2}{\alpha}$, where l is the characteristic distance of heat transport and α is the thermal diffusivity of materials (for most organic materials, $\alpha \sim 10^{-7}$ m^2/s). Therefore, the time needed for the quasi-equilibrium between heat generation and conduction is on the order of 10^{-5} s ($l \sim 10^{-6}$ m, corresponding to the length scale of the heating region). After the quasi-equilibrium sets up, the temperature will undergo a slow and steady rise since a large portion of the generated energy is diffused into adjacent regions. In the high laser power case (Figure 3a), the temperature threshold can be reached during the initial fast increase stage across the whole probed region; therefore, the total response time is short; in the low laser power case (Figure 3d), the initial fast response (from 0 to ~10 μs) cannot reach the temperature threshold throughout the whole probed region, and the following gradual heating will take up to 50 μs to achieve full dissolution throughout the film thickness. Note that there is no gradual heating stage in the high laser power case due to the fact that the absorbance of the dissolved matter is extremely low after the phase transition. The apparent slow temperature increase after it passes 304 K is due to the heat conduction from the heat flux at the silicon surface; otherwise, the temperature would drop gradually. The gradual temperature increase induced by the heat flux can also be seen in case (b), from the temperature increase of the two center points (A and B).

Figure 3b,e shows the temperature field profiles (from left to right) in the beginning, near the full dissolution of the probed region, and in the end of the simulation. As shown in Figure 3g, the domain with z from 0.05 μm up to 1 mm (not shown fully) is the solvent THF and region with z ranging from 0 to 0.05 μm is the P3HT:F4TCNQ thin film domain, with the silicon dioxide layer (−0.05 to ~0 μm) and the silicon with z from −0.05 μm down to −1 mm (not shown fully) underneath. Note that the temperature scales in the two figures are set differently for better clarity of each temperature field. In general, the short high-power pulse (Figure 3b) induced a much larger temperature increase field in a more confined region, compared with the long low-power pulse (Figure 3e). The difference of the temperature contour shape evolution comes from the fact that, in the low-power case, the irradiated region of the P3HT film stays much longer before it dissolves such that it generates more heat and affects a larger adjacent region, notably the solvent domain ($z > 0.05$ μm).

Figure 3c,f illustrates the phase transition evolution during the dissolution in terms of the phase transition factor α with a value between 0 (no transition) and 1 (full transition). In both cases, the dissolution is fast in the beginning and slows down quickly later, which agrees well with the experimental observation. The short high-power pulse leads to a sharp edge around the dissolved region, while the long low-power pulse results in a much wider edge, reducing the fidelity of the pattern. The wider edge feature comes from fact that the two adjacent media, THF and SiO_2, have different thermal effusivities (e), which measure the material's ability to exchange thermal energy with its surroundings ($e = \sqrt{\kappa\rho c}$, where κ, ρ, and c denote thermal conducticity, mass density, and specific heat capacity, respectively). THF has smaller thermal effusivity and is thus less efficient in transporting heat from the heated P3HT film. Therefore, the points at the top surface of P3HT will have higher temperature than the points at the bottom surface with the same radial position before the corresponding local elements dissolve. For example, as shown in Figure 3d, the temperature of point D (0.05, 5) is always higher than that of point C (0, 5). Such a temperature difference between the two interfaces of the original P3HT domain results in the asymmetrical edge shape of the dissolved region (wider at the top interface). However, for the high-power case, due to the significantly faster dissolution of the P3HT film, the heat diffusion into adjacent media is limited and does not bring any notable asymmetry in temperature distribution between the two interfaces; thus, the dissolved region has a sharp edge. The above analysis also indicates that, in both cases, the heat flux on the surface of silicon does not affect the dissolution process in any noticeable way; otherwise, the dissolved region would have an asymmetrical edge with a wider opening at the bottom interface. This is because the timescale for sufficient thermal diffusion from the heat flux underneath the SiO_2 layer to the dissolved region is longer than the dissolution time in both cases. This also justifies the self-consistency of our previous assumption that the volumetric absorbance of the laser energy in the silicon substrate can be lumped into a surface heat flux.

Figure 3h shows the comparison between the experimental and simulation results for the whole power range measured in our experiment. In general, our model is in good agreement with the measured data. Both the model and data show the two timescales for the thermal dissolution and agree on the threshold optical flux to change from the slow to the fast dissolution process. The discrepancy between the model and data is mainly due to the simplifications in the simulation; for example, the energy losses due to interface thermal resistance and thermal radiation are not included. Nevertheless, this model is sufficient to predict the dissolution timescale as a function of optical intensity. Note that, with sufficiently high optical intensity, the photothermal mechanism can efficiently etch the P3HT film with a characteristic length of 1 μm within 1 μs, corresponding to a high writing speed of 1 m/s.

The mechanism of the temperature-induced phase transition can be understood in the following way: the equilibrium phase distribution in any solute-solvent system depends on the minimization of the Gibbs free energy of the system. For the P3HT:F4TCNQ-THF system, at room temperature, the Gibbs free energy change for mixing (ΔG_{mix}) is positive, and thus, the thermodynamic equilibrium keeps the doped polymer film from dissolving into the solvent. $\Delta G_{mix} = \Delta H_{mix} - T\Delta S_{mix}$, where ΔH_{mix} and ΔS_{mix} are both positive and independent of temperature (at least in the small temperature range). With increased temperature, the second term, $T\Delta S_{mix}$, drives ΔG_{mix} through zero to negative values, and thereafter, the dissolution (mixing) becomes spontaneous. The chemophysical mechanism here is still under investigation. One possible explanation is that, as the temperature increases, thermally excited F4TCNQ* reacts with THF solvent molecules to form a neutral, nondoping, and highly soluble F4TCNQ-THF complex. Hence, ionized F4TCNQ is removed from the P3HT indirectly by depletion of the neutral F4TCNQ; that is, the [polymer$^+$]:[dopant$^-$] complex is forced to return to being neutral polymer and dopant molecules, resulting in the dissolution of P3HT into the good solvent THF. A similar photochemical mechanism via the same F4TCNQ-THF complex formation has been reported.[34]

As discussed in the Introduction, we have previously shown that a photochemical reaction occurs with irradiation of 405 nm light but not with 532 nm light. With the new thermal

DOI: 10.1021/acsami.9b15860
ACS Appl. Mater. Interfaces 2019, 11, 41717−41725

model shown here, we are able to predict the photothermal dissolution rate. Now, we utilize the model to quantify the relative contributions from photothermal and photochemical dissolution with a 405 nm laser. Figure 4 shows the AFM

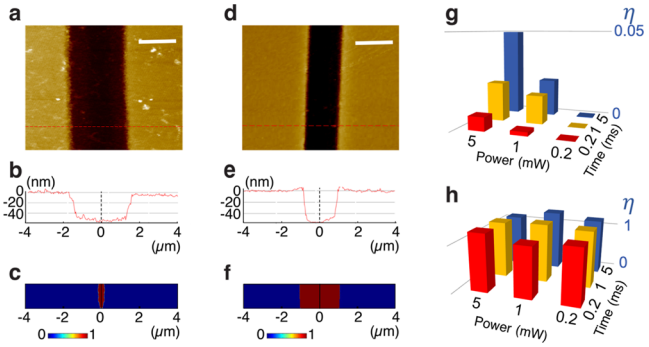

Figure 4. (a) AFM measurement of the line patterned by 405 nm laser; scale bar, 2 μm. (b) cross section profile along the dashed red line in panel (a), showing a line width of 3.2 μm (evaluated at the surface of the film). (c) Simulation results of the phase transition factor (α) profile assuming the photothermal mechanism only, showing a 0.4 μm line width. (d–f) Results for the line patterned by 532 nm laser. (g) The ratio of the predicted over measured dissolution volumes (η) over a wide range of laser powers and dwell times for lines patterned by 405 nm laser, showing the contribution from the photothermal effect is negligible (below 5%). (h) η for lines patterned by the 532 nm laser is close to 1 within the whole range.

images of P3HT:F4TCNQ films that were etched with the (a) 405 nm laser and (d) 532 nm laser. The laser power is 1 mW (measured after a 50× objective lens with a focus waist of 3.3 μm in diameter, corresponding to an average intensity of 11.7 kW/cm^2), and the writing speed is 1 mm/s, corresponding to a dwell time of 3.3 ms, which is long enough to allow full dissolution even assuming the slow dissolution mechanism. As mentioned above, our method can intrinsically achieve a writing speed of 1 m/s, but due to practical limitations, for example, the movement instability of the nanopositioning stage that mounts the sample, we choose a relatively low writing speed, 1 mm/s. Nevertheless, such speed is already adequately high compared with previous results, 0.01–0.1 mm/s.[3] With better instrumentation, for instance, using a scanning Galvo mirror system rather than a nanopositioning stage, it is easy to realize the extra high speed up to 1 m/s. Figure 4b,e shows the cross section profiles along the dashed red lines in panels (a) and (d), respectively. The writing resolution is 2.0 μm for a 532 nm laser, but it is 3.2 μm for a 405 nm laser. In both cases, the irradiated regions are fully etched, although the 405 nm laser results in a relatively sharper edge.

Next, we use the thermal model to calculate the dissolution of both samples assuming the photothermal mechanism only. The cross sections of the predicted laser etching show very different etch widths for irradiation with 405 nm (Figure 4c) versus 532 nm light (Figure 4f). Such a difference directly comes from the different volumetric absorbance in the P3HT:F4TCNQ film, which is 0.41 for 532 nm and only 0.14 for 405 nm (Figure S3). The predicted etch width of 1.8 μm matches very closely to the measured 2.0 μm for the 532 nm laser, which involves only the photothermal mechanism, confirming the reliability of the model. However, the prediction of the etch width for the 405 nm laser is only 0.4 μm, presenting an obvious discrepancy with the AFM measured result, 3.2 μm. Figure 4g,h shows the ratio of the predicted over measured dissolution volumes (η) as a function of the laser power and dwell time. For the lines patterned by the 405 nm laser (Figure 4g), across the whole experimental parameter range, only <5% of the volumetric dissolution occurs as a result of the photothermal process and >95% of the dissolution occurs due to the previously reported photochemical process. In contrast, with 532 nm irradiation, η is close to 1 for the whole experimental range. Our results show that the previous assumption that only particular laser wavelengths could result in dissolution of doped polymer films is only valid for very low laser intensities (typically <10 kW/cm^2).[34] Absorbance at any wavelength within the polymer:dopant absorbance spectrum will result in heating. If the heating reaches above a threshold (304 K for P3HT:F4TCNQ in THF), then the film will dissolve, offering a new avenue for high-speed patterning of doped polymers.

For 405 nm irradiation, the photochemical mechanism dominates the laser-induced dissolution, particularly when low laser intensities (1–15 kW/cm^2) and long dwell times are utilized. Although the writing resolution was "worsened" by the photochemical effect in the experiment shown in Figure 4, it is critical to reiterate that the resolution could have been substantially improved by using less laser intensities (around 1 kW/cm^2 for 405 nm lasers) as previously reported.[1,2] The photochemical removal of dopants reduces the dopant concentration in the P3HT and thus lowers the temperature needed to dissolve a particular volume element to well below 304 K. Therefore, it was possible to achieve sub-diffraction resolution and features down to 200 nm in previous experiments with 405 nm irradiation. Thus, understanding these mechanisms also lays the foundation for ultraprecise laser direct writing and simultaneous minimization of unwanted thermal degradation on adjacent layers in multilayer systems, which are common for polymeric electronics, such as thin film transistors, solar cells, and flexible displays.

The quantitative mechanistic understanding of how different dissolution mechanisms contribute to the dissolution rate is critical to expanding the use of laser writing for the patterning of organic electronic semiconductors. All of the processes described here are at very low temperature (≤304 K) with rapid write times, low laser intensities, and no destruction (bond-breaking) anywhere in the film. In addition, no cross-linking (bond forming) is necessary to affect the patterning. This combination of positive features makes the DISC-based optical patterning a very attractive method to pattern organic electronic circuits.

CONCLUSIONS

In this work, we study the mechanism of photothermal etching of doped polymer films, specifically P3HT:F4TCNQ immersed in the THF environment. We utilize a time-resolved in situ optical probing technique to probe the dynamic changes of the reflectance of the polymer-dopant-solvent system in order to quantify the dissolution rate of the P3HT:F4TCNQ thin films upon photothermal irradiation. We find that, in addition to the photochemical mechanism previously reported, a temperature increase can also induce the dissolution of the P3HT:F4TCNQ thin film in THF. A threshold temperature of 304 K is confirmed for the thermal mechanism. We show the existence of the two distinct timescales for the thermal dissolution in a wide range of laser intensities, corresponding to fast and slow thermal responses of the system. An associated

DOI: 10.1021/acsami.9b15860
ACS Appl. Mater. Interfaces 2019, 11, 41717–41725

heat transfer model supports the purely photothermal effect as the mechanism underlying these experimental results, which in return help to verify the reliability and accuracy of the thermal modeling. The thermal modeling is then used to estimate the contributions from the photothermal effect of the 405 nm laser irradiation where both photothermal and photochemical mechanisms are present. Our results indicate that the photochemical mechanism contributes to >95% of the etch rate for low-intensity 405 nm light, which implies that the photochemical mechanism lowers the dissolution temperature of P3HT:F4TCNQ in THF. Besides, with good control of laser intensity and write speed, the photothermal mechanism can yield a much faster etch rate without inducing large temperature changes (<10 K), regardless of the laser wavelength. Minimizing temperature changes will allow organic layers to be patterned even within multilayer organic stacks without inducing thermal dissolution of adjacent layers. We envision that the DISC-based laser direct writing approach will boost the development of organic electronics.

EXPERIMENTAL SECTION

Materials. P3HT (Plextronics, molecular weight = 65 kDa) was purchased from Sigma-Aldrich. F4TCNQ was purchased from TCI (98+ %). Solvents were purchased from Sigma-Aldrich and dried over 3A molecular sieves. Acetonitrile was degassed by sonication under vacuum for 10 min and then stored under nitrogen. All other materials were used as received.

Sample Preparation. 1 × 1 cm silicon substrates with a layer of 300 nm thick hydrothermal-grown silicon dioxide on top were cleaned by sequential sonication steps in acetone, 10% Mucasal:-deionized (DI) water, and DI water, blown dry with compressed nitrogen, and UV-ozone-treated for 30 min before use. P3HT (10 mg/mL, chlorobenzene (CB)) solutions were heated to 60 °C and left to dissolve overnight. F4TCNQ solutions (0.1 mg/mL, AN or 0.3 mg/mL, CB) were prepared at room temperature in acetonitrile (AN) or at 60 °C in CB and cooled to room temperature shortly before use. Thin films of P3HT were spin-coated on silicon substrates from 60 °C solutions at 1000 rpm until dry. Films were sequentially doped from F4TCNQ:AN, as previously described.[2] Doped films were 50 nm thick, as measured by a profilometer (Dektak 150). Films on substrates are sealed in a customized solvent cell with THF, as shown in Figure 1b. All sample preparation was performed in a nitrogen glovebox (<3 ppm H_2O, O_2) equipped with a molecular sieve solvent trap.

Time-Resolved In Situ Optical Probing. As shown in Figure 1, a dual-beam strategy was utilized for simultaneous processing and probing. The processing laser beam (532) from a 532 nm continuous-wave (CW) laser (Sprout-D, from Lighthouse Photonics) passes through an acousto-optic modulator (AOM) and is split by an 8:2 nonpolarized beam splitter (NPBS); the minor branch is collected by a photodetector (PD), and the major branch is delivered through a neutral density filter (ND) and a mechanical shutter (MS), reflected off a dichroic mirror (DM), and then focused by a long-working-distance 10× objective lens (OL, Mitutoyo Plan Apo infinity corrected objective) onto the sample (SM), through the coverslip and solvent at the interface between the film and the silicon substrate. The probing laser (633) is from a 633 nm CW laser (helium-neon laser, from Newport), and its s-polarized portion is reflected off a polarized beam splitter cube (PBS, from Thorlabs), through a quarter wave plate (QWP), focused through the same OL onto the sample. The reflected 633 nm light from the sample is collected by the OL, passing the QWP again, becomes p-polarized, and is transmitted through the PBS; the signal passes a 532 nm notch filter (NF) and is collected by another PD. The signals from the two PDs are sent to and synchronized by an oscilloscope (OS) controlled by a home-built Lab-view program. The sample is mounted on a programmable nanopositioning piezo stage (PS, from Aerotech). A charge-coupled device (CCD) camera system is coupled with the transmitted lights (both 532 and 633 nm) through the DM and NPBS, for alignment, focusing, and monitoring of the dynamic process online.

ASSOCIATED CONTENT

Supporting Information

The Supporting Information is available free of charge on the ACS Publications website at DOI: 10.1021/acsami.9b15860.

Knife edge measurement of the laser beam spot size, optical properties of the P3HT:F4TCNQ thin film by ellipsometry measurement, transfer matrix method to calculate the absorbance in P3HT and substrate, dissolution temperature measurement results of P3HT:F4TCNQ thin film immersed in THF, temperature field and dissolution progress calculated with surface heat flux at the interface of silicon dioxide and silicon (PDF)

AUTHOR INFORMATION

Corresponding Authors

*E-mail: amoule@ucdavis.edu (A.J.M.).
*E-mail: cgrigoro@berkeley.edu (C.P.G.).

ORCID

Adam J. Moulé: 0000-0003-1354-3517
Costas P. Grigoropoulos: 0000-0002-8505-4037

Author Contributions

The manuscript was written through contributions of all authors. All authors have given approval to the final version of the manuscript.

Notes

The authors declare no competing financial interest.

ACKNOWLEDGMENTS

This work was funded by the National Science Foundation Scalable Nanomanufacturing Program, Award # CMMI 1636385. Z.I.B.-V. acknowledges the SENER-CONACyT program for funding, Project # 291145.

REFERENCES

(1) Jacobs, I. E.; Li, J.; Burg, S. L.; Bilsky, D. J.; Rotondo, B. T.; Augustine, M. P.; Stroeve, P.; Moulé, A. J. Reversible Optical Control of Conjugated Polymer Solubility with Sub-Micrometer Resolution. *ACS Nano* **2015**, *9*, 1905−1912.

(2) Jacobs, I. E.; Moulé, A. J. Controlling Molecular Doping in Organic Semiconductors. *Adv. Mater.* **2017**, *29*, 1703063.

(3) Jacobs, I. E.; Aasen, E. W.; Nowak, D.; Li, J.; Morrison, W.; Roehling, J. D.; Augustine, M. P.; Moulé, A. J. Direct-Write Optical Patterning of P3HT Films Beyond the Diffraction Limit. *Adv. Mater.* **2017**, *29*, 1603221.

(4) Sun, Y.; Rogers, J. A. Inorganic Semiconductors for Flexible Electronics. *Adv. Mater.* **2007**, *19*, 1897−1916.

(5) Zang, Y.; Shen, H.; Huang, D.; Di, C.-A.; Zhu, D. A Dual-Organic-Transistor-Based Tactile-Perception System with Signal-Processing Functionality. *Adv. Mater.* **2017**, *29*, 1606088.

(6) Berggren, M.; Nilsson, D.; Robinson, N. D. Organic Materials for Printed Electronics. *Nat. Mater.* **2007**, *6*, 3−5.

(7) Sanvito, S. Organic Electronics: Spintronics Goes Plastic. *Nat. Mater.* **2007**, *6*, 803.

(8) Klauk, H. *Organic Electronics: Materials, Manufacturing, and Applications*; 1st ed.; John Wiley & Sons: NJ, 2016.

(9) So, F. *Organic Electronics: Materials, Processing, Devices and Applications*; 1st ed.; CRC press: FL, 2009.

(10) Sekitani, T.; Someya, T. Stretchable, Large-Area Organic Electronics. *Adv. Mater.* **2010**, *22*, 2228−2246.

DOI: 10.1021/acsami.9b15860
ACS Appl. Mater. Interfaces 2019, 11, 41717−41725

(11) Gundlach, D. J. Organic Electronics: Low Power, High Impact. *Nat. Mater.* **2007**, *6*, 173.
(12) Arias, A. C.; MacKenzie, J. D.; McCulloch, I.; Rivnay, J.; Salleo, A. Materials and Applications for Large Area Electronics: Solution-Based Approaches. *Chem. Rev.* **2010**, *110*, 3−24.
(13) Li, J.; Zhang, G.; Holm, D. M.; Jacobs, I. E.; Yin, B.; Stroeve, P.; Mascal, M.; Moulé, A. J. Introducing Solubility Control for Improved Organic P-Type Dopants. *Chem. Mater.* **2015**, *27*, 5765−5774.
(14) Jacobs, I. E.; Aasen, E. W.; Oliveira, J. L.; Fonseca, T. N.; Roehling, J. D.; Li, J.; Zhang, G.; Augustine, M. P.; Mascal, M.; Moulé, A. J. Comparison of Solution-Mixed and Sequentially Processed P3HT:F4TCNQ Films: Effect of Doping-Induced Aggregation on Film Morphology. *J. Mater. Chem. C* **2016**, *4*, 3454−3466.
(15) Jacobs, I. E.; Wang, F.; Hafezi, N.; Medina-Plaza, C.; Harrelson, T. F.; Li, J.; Augustine, M. P.; Mascal, M.; Moulé, A. J. Quantitative Dedoping of Conductive Polymers. *Chem. Mater.* **2017**, *29*, 832−841.
(16) Kwon, H.-J.; Yeo, J.; Jang, J. E.; Grigoropoulos, C. P.; Yoo, J.-H. Single Pass Laser Process for Super-Hydrophobic Flexible Surfaces with Micro/Nano Hierarchical Structures. *Materials* **2018**, *11*, 1226.
(17) Xing, G.; Mathews, N.; Lim, S. S.; Yantara, N.; Liu, X.; Sabba, D.; Grätzel, M.; Mhaisalkar, S.; Sum, T. C. Low-Temperature Solution-Processed Wavelength-Tunable Perovskites for Lasing. *Nat. Mater.* **2014**, *13*, 476.
(18) Ko, S. H.; Pan, H.; Grigoropoulos, C. P.; Luscombe, C. K.; Fréchet, J. M. J.; Poulikakos, D. All-Inkjet-Printed Flexible Electronics Fabrication on a Polymer Substrate by Low-Temperature High-Resolution Selective Laser Sintering of Metal Nanoparticles. *Nanotechnology* **2007**, *18*, 345202.
(19) Rigas, G.-P.; Payne, M. M.; Anthony, J. E.; Horton, P. N.; Castro, F. A.; Shkunov, M. Spray Printing of Organic Semiconducting Single Crystals. *Nat. Commun.* **2016**, *7*, 13531.
(20) Fukuda, K.; Takeda, Y.; Yoshimura, Y.; Shiwaku, R.; Tran, L. T.; Sekine, T.; Mizukami, M.; Kumaki, D.; Tokito, S. Fully-Printed High-Performance Organic Thin-Film Transistors and Circuitry on One-Micron-Thick Polymer Films. *Nat Commun.* **2014**, *5*, 4147.
(21) An, B. W.; Kim, K.; Lee, H.; Kim, S. Y.; Shim, Y.; Lee, D. Y.; Song, J. Y.; Park, J. U. High-Resolution Printing of 3D Structures Using an Electrohydrodynamic Inkjet with Multiple Functional Inks. *Adv. Mater.* **2015**, *27*, 4322−4328.
(22) Kwon, J.; Takeda, Y.; Fukuda, K.; Cho, K.; Tokito, S.; Jung, S. Three-Dimensional, Inkjet-Printed Organic Transistors and Integrated Circuits with 100% Yield, High Uniformity, and Long-Term Stability. *ACS Nano* **2016**, *10*, 10324−10330.
(23) Lee, W.-J.; Park, W.-T.; Park, S.; Sung, S.; Noh, Y.-Y.; Yoon, M.-H. Large-Scale Precise Printing of Ultrathin Sol−Gel Oxide Dielectrics for Directly Patterned Solution-Processed Metal Oxide Transistor Arrays. *Adv. Mater.* **2015**, *27*, 5043−5048.
(24) Skrypnychuk, V.; Wetzelaer, G.-J. A. H.; Gordiichuk, P. I.; Mannsfeld, S. C. B.; Herrmann, A.; Toney, M. F.; Barbero, D. R. Ultrahigh Mobility in an Organic Semiconductor by Vertical Chain Alignment. *Adv. Mater.* **2016**, *28*, 2359−2366.
(25) Vyas, V. S.; Lau, V. W.-H.; Lotsch, B. V. Soft Photocatalysis: Organic Polymers for Solar Fuel Production. *Chem. Mater.* **2016**, *28*, 5191−5204.
(26) Zhuang, X.; Mai, Y.; Wu, D.; Zhang, F.; Feng, X. Two-Dimensional Soft Nanomaterials: a Fascinating World of Materials. *Adv. Mater.* **2015**, *27*, 403−427.
(27) Kim, J.; Park, H. J.; Grigoropoulos, C. P.; Lee, D.; Jang, J. Solution-Processed Nickel Oxide Nanoparticles with NiOOH for Hole Injection Layers of High-Efficiency Organic Light-Emitting Diodes. *Nanoscale* **2016**, *8*, 17608−17615.
(28) Yalisove, S. M.; Sugioka, K.; Grigoropoulos, C. P. Advances and Opportunities of Ultrafast Laser Synthesis and Processing. *MRS Bull.* **2016**, *41*, 955−959.
(29) Yeo, J.; Hong, S.; Kim, G.; Lee, H.; Suh, Y. D.; Park, I.; Grigoropoulos, C. P.; Ko, S. H. Laser-Induced Hydrothermal Growth of Heterogeneous Metal-Oxide Nanowire on Flexible Substrate by Laser Absorption Layer Design. *ACS Nano* **2015**, *9*, 6059−6068.
(30) Jeon, H.; Schmidt, R.; Barton, J. E.; Hwang, D. J.; Gamble, L. J.; Castner, D. G.; Grigoropoulos, C. P.; Healy, K. E. Chemical Patterning of Ultrathin Polymer Films by Direct-Write Multiphoton Lithography. *J. Am. Chem. Soc.* **2011**, *133*, 6138−6141.
(31) Choi, J.; Koo, S.; Sakellari, I.; Kim, H.; Su, Z.; Carter, K. R.; Farsari, M.; Grigoropoulos, C. P.; Russell, T. P. Guided Assembly of Block Copolymers in Three-Dimensional Woodpile Scaffolds. *ACS Appl. Mater. Interfaces* **2018**, *10*, 42933−42940.
(32) Ko, S. H.; Pan, H.; Grigoropoulos, C. P.; Fréchet, J. M. J.; Luscombe, C. K.; Poulikakos, D. Lithography-Free High-Resolution Organic Transistor Arrays on Polymer Substrate by Low Energy Selective Laser Ablation of Inkjet-Printed Nanoparticle Film. *Appl. Phys. A: Mater. Sci. Process.* **2008**, *92*, 579−587.
(33) Bäuerle, D. *Laser Processing and Chemistry*; 4th ed.; Springer: NY, 2013.
(34) Fuzell, J.; Jacobs, I. E.; Ackling, S.; Harrelson, T. F.; Huang, D. M.; Larsen, D.; Moulé, A. J. Optical Dedoping Mechanism for P3HT/F4TCNQ Mixtures. *J. Phys. Chem. Lett.* **2016**, *7*, 4297−4303.
(35) Petsch, T.; Haenel, J.; Clair, M.; Keiper, B.; Scholz, C. Laser Processing of Organic Photovoltaic Cells with a Roll-to-Roll Manufacturing Process. In *Laser-based Micro-and Nanopackaging and Assembly V*; International Society for Optics and Photonics: 2011, *7921*, p 79210,.
(36) Katsidis, C. C.; Siapkas, D. I. General Transfer-Matrix Method for Optical Multilayer Systems with Coherent, Partially Coherent, and Incoherent Interference. *Appl. Opt.* **2002**, *41*, 3978−3987.

DOI: 10.1021/acsami.9b15860
ACS Appl. Mater. Interfaces 2019, 11, 41717−41725